



**Michigan
Technological
University**

Michigan Technological University
Digital Commons @ Michigan Tech

Michigan Tech Publications

6-6-2022

Utilization of Bayesian Optimization and KWN Modeling for Increased Efficiency of Al-Sc Precipitation Strengthening

Kyle Deane

Michigan Technological University, kjdeane@mtu.edu

Yang Yang

Michigan Technological University, yyang7@mtu.edu

Joseph Licavoli

Michigan Technological University, jjlicavo@mtu.edu

Vu Nguyen

Deakin University

Santu Rana

Deakin University

See next page for additional authors

Follow this and additional works at: <https://digitalcommons.mtu.edu/michigantech-p>



Part of the [Materials Science and Engineering Commons](#)

Recommended Citation

Deane, K., Yang, Y., Licavoli, J., Nguyen, V., Rana, S., Gupta, S., Venkatesh, S., & Sanders, P. G. (2022). Utilization of Bayesian Optimization and KWN Modeling for Increased Efficiency of Al-Sc Precipitation Strengthening. *Metals*, 12(6). <http://doi.org/10.3390/met12060975>
Retrieved from: <https://digitalcommons.mtu.edu/michigantech-p/16227>

Follow this and additional works at: <https://digitalcommons.mtu.edu/michigantech-p>



Part of the [Materials Science and Engineering Commons](#)

Authors

Kyle Deane, Yang Yang, Joseph Licavoli, Vu Nguyen, Santu Rana, Sunil Gupta, Svetha Venkatesh, and Paul G. Sanders

Article

Utilization of Bayesian Optimization and KWN Modeling for Increased Efficiency of Al-Sc Precipitation Strengthening

Kyle Deane ¹, Yang Yang ^{1,*}, Joseph J. Licavoli ¹, Vu Nguyen ², Santu Rana ², Sunil Gupta ², Svetha Venkatesh ² and Paul G. Sanders ^{1,*}

¹ Department of Materials Science & Engineering, Michigan Technological University, Houghton, MI 49931, USA; kjdeane@mtu.edu (K.D.); jjlicavo@mtu.edu (J.J.L.)

² The Applied Artificial Intelligence Institute, Deakin University, Geelong, VIC 3220, Australia; v.nguyen@deakin.edu.au (V.N.); santu.rana@deakin.edu.au (S.R.); sunil.gupta@deakin.edu.au (S.G.); svetha.venkatesh@deakin.edu.au (S.V.)

* Correspondence: yyang10@mtu.edu (Y.Y.); sanders@mtu.edu (P.G.S.); Tel.: +1-906-487-2339 (P.G.S.)

Abstract: The Kampmann and Wagner numerical model was adapted in MATLAB to predict the precipitation and growth of Al₃Sc precipitates as a function of starting concentration and heat-treatment steps. This model was then expanded to predict the strengthening in alloys using calculated average precipitate number density, radius, etc. The calibration of this model was achieved with Bayesian optimization, and the model was verified against experimentally gathered hardness data. An analysis of the outputs from this code allowed the development of optimal heat treatments, which were validated experimentally and proven to result in higher final strengths than were previously observed. Bayesian optimization was also used to predict the optimal heat-treatment temperatures in the case of limited heat-treatment times.

Keywords: KWN; Bayesian optimization; precipitation strengthening; scandium; trialuminide



Citation: Deane, K.; Yang, Y.; Licavoli, J.J.; Nguyen, V.; Rana, S.; Gupta, S.; Venkatesh, S.; Sanders, P.G. Utilization of Bayesian Optimization and KWN Modeling for Increased Efficiency of Al-Sc Precipitation Strengthening. *Metals* **2022**, *12*, 975. <https://doi.org/10.3390/met12060975>

Academic Editor: Cristiano Fragassa

Received: 31 March 2022

Accepted: 31 May 2022

Published: 6 June 2022

Publisher's Note: MDPI stays neutral with regard to jurisdictional claims in published maps and institutional affiliations.



Copyright: © 2022 by the authors. Licensee MDPI, Basel, Switzerland. This article is an open access article distributed under the terms and conditions of the Creative Commons Attribution (CC BY) license (<https://creativecommons.org/licenses/by/4.0/>).

1. Introduction

Al-Sc precipitation strengthening alloys have been proven in the literature to have excellent coarsening resistance when compared to more traditional precipitation strengthening alloys due, in large part, to the low diffusion rates and low solubility limits of Sc in aluminum [1–3]. The formation of nano-sized, nearly spherical L₁₂ Al₃Sc has shown promising precipitation strengthening at ambient and elevated temperatures [3,4]. However, due to the scarcity and expense of Sc, little work has been performed to experimentally optimize heat treatments in various Al-Sc alloys. The goal of the current study is to outline and verify a computational method to accurately predict Al₃Sc precipitate nucleation and growth. This information is then tied to strengthening models to estimate optimal heat-treatment schedules, which were also evaluated experimentally.

Many thermodynamic and kinetic modeling packages used in materials science contain precipitation-strengthening models that can give rough estimates for optimal material chemistry and processing parameters. The primary issue is that these models are designed for “generality”, which favors the use of few fitting parameters and limited system-specific knowledge at the expense of accuracy. For example, models involving temperature dependence often adopt Arrhenius relations, requiring several fitting parameters (pre-exponential factors, exponential constants, etc.) to “capture” the underlying physics without explicitly deriving the true and complex relations that govern the value of these fitting parameters for a specific material system. The user is then tasked with finding the proper fitting parameters to match their system of interest. There are obvious practical incentives to adopt this approach, including time constraints, limitations on theory, and limits on computational resources, but the incentives for making these assumptions can often be overwhelmed by the inadequacy of the resulting models and the faulty assertions flowing from them. To

remedy this problem, one may develop a modeling method that rapidly and automatically identifies key fitting parameters from existing data sets in the literature or from material databases, thus retaining generality without sacrificing as much accuracy. Such a model would require correlation with real experimental data to give meaningful results due to the complexity of the thermodynamic and kinetic simulations, but, given enough pre-existing data, an ample amount of inputs can be adjusted to fine-tune the result, enabling higher accuracy and increasing the likelihood of achieving an optimized process.

To accomplish this goal, an implementation of Kampmann and Wagner's numerical precipitation model (hereafter referred to as the KWN model) was developed to approximate the experimental conditions reported in this work, as well as those found in [5]. The KWN model tracks precipitate nucleation, growth, coarsening, and dissolution over a series of discrete timesteps by iteratively solving classical nucleation theory and Gibbs–Thomson relationship equations. The precipitates formed are grouped into bins of similar radii and are allowed to grow or dissolve in accordance with their size in the equations at each timestep [6–8].

The KWN model involves many tunable configuration parameters. These parameters can result in significant improvements in accuracy if they are fitted properly. Bayesian optimization (BO) is a powerful tool for the optimization of complex systems. It offers greater automation to increase both product quality and productivity [9–11]. BO was therefore used to fit the parameters for the KWN model to better coincide with the experimental results. Once the parameters were properly fitted, BO was of further use in identifying the heat treatments with the model that would yield the greatest strength.

2. Materials and Methods

The following components, described in detail in Sections 2.1–2.3, were integral to this study:

1. **Precipitation and Strengthening Model**—By simulating nucleation and growth of Al_3Sc in Al–Sc binary alloys, this program predicts strengthening behavior with aging.
2. **Experimental Verification**—Casting, aging, and hardness testing of Al–Sc binary alloys generated data for fitting and verification of the precipitation and strengthening model.
3. **Bayesian Optimization**—Bayesian optimization (BO) was used to obtain the best fit between experimentally observed and simulated strengthening behavior. After the model was calibrated, BO was used again to suggest heat treatments for optimal strengthening.

2.1. Precipitation and Strengthening Model

The precipitation and strengthening model, essentially a modified KWN model with strengthening equations in the form of a MATLAB program, can be separated into several distinct sections, as shown in Figure 1: initial material and process-specific inputs (Section 2.1.1), an outer loop that iterates for each heat-treatment temperature (Section 2.1.2), an inner loop that iterates through the time of each heat-treatment step and calculates precipitate nucleation behavior at each timestep (Section 2.1.3), and the innermost loop that adjusts the precipitate radii formed in previous timesteps according to the Gibbs–Thomson relationship (Section 2.1.4). After all nucleation, growth, and dissolution are calculated for a given timestep, solute concentration is adjusted for solute atoms lost to or gained from precipitates.

2.1.1. Model Inputs

In the first section of the model code, all inputs are defined, and constants related to these values are calculated. Process-specific inputs include the number, temperature, and length of heat-treatment steps, as well as the initial solute concentration of the alloy in question. Material-specific inputs include Gibbs free energy data for calculation of the solvus line [12], the diffusion coefficient of the solute atoms in the matrix (D_0), the vacancy formation and migration energies of the solute atoms (E_f^{v-X} and E_m^v), lattice parameters of the matrix and precipitate phase (a_m

and a_p), Poisson's ratio of the matrix and precipitate phase (ν_m and ν_p), and shear modulus of the matrix and the precipitate phase (G_m^{shear} and G_p^{shear}).

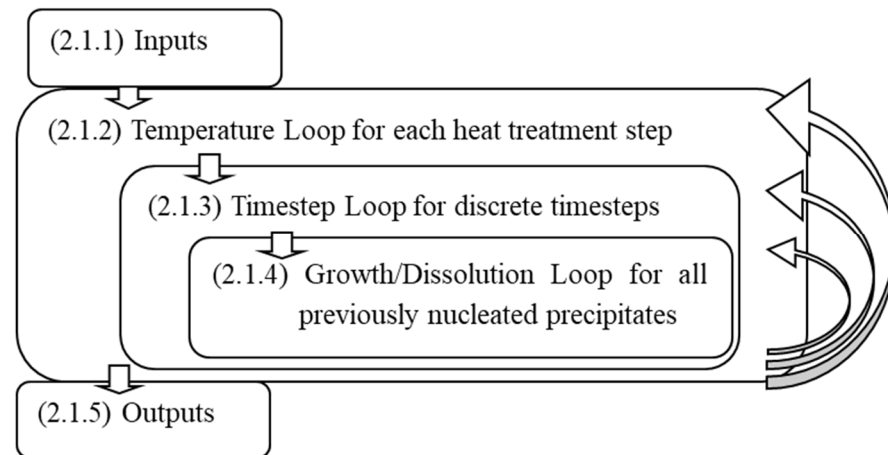


Figure 1. Visual representation of the distinct sections of the precipitation and strengthening model. The model itself is available in the Supplementary Material.

2.1.2. Model Temperature Loop

Following the input section, a loop is entered to calculate temperature-dependent values for the first heat-treatment step. This loop repeats whenever the simulated heat-treatment time expires and the temperature is raised or lowered to the next listed heat-treatment temperature.

The first part of the temperature loop calculates the Al-intermetallic solvus line, defining the solubility of the solute atoms in the matrix. As the temperature increases, so does the solubility, which can cause significant precipitate dissolution at the beginning of a relatively high heat-treatment step. The composition of the solvus line was found at each temperature using the Gibbs free energy curve data from the input section [12].

The second part of the Temperature Loop calculates the diffusivity of the solute atom in the matrix, as seen in Equation (1) [13], where D_0 is the diffusion coefficient, f is the dimensionless correlation factor (0.7815 for FCC materials), E_f^{v-X} is the vacancy formation energy near an impurity atom X , and E_m^v is the impurity migration energy mediated by a vacancy [14]. As the temperature increases, the diffusion rates of solute atoms increase, accelerating nucleation and growth kinetics.

$$D = D_0 f \exp\left(\frac{-E_f^{v-X} - E_m^v}{k_B T}\right) \quad (1)$$

Once diffusivity is calculated, a nested loop is entered to perform all time-dependent calculations.

2.1.3. Model Timestep Loop

There is a large loop within the outer temperature loop that iterates for each timestep. This loop holds all time-dependent constitutive equations and tracks solute concentration evolution, as affected by nucleation and growth. At each timestep, the critical radius of precipitate nucleation and nucleation rate are calculated based on the solute concentration at the beginning of the step. Another loop (discussed in the next section) is then entered to grow/dissolve precipitates made in previous steps, and, next, the solute concentration is updated to account for all solute loss or gain from the precipitates. At the end of each timestep, the average precipitate radius and corresponding strength prediction is outputted.

In order to determine the critical radius of the precipitate nucleation, it is important to know the changes in Gibbs free energy associated with creating new precipitate volume (ΔG_v) as well

as creating a greater matrix-precipitate interfacial area (ΔG_s). Equations (2) and (3) demonstrate the main equations used to determine these values, with $\Delta G_{Al_3X}^{formation}$ as the Gibbs energy in formation of Al_3X , $G_{matrix}^{Al_3X}$ as the intercept at 25%X of a line tangential to the matrix-phase Gibbs energy curve at the current matrix composition [15], ε as the misfit strain between the two phases, G_m^{shear} or G_p^{shear} as the shear modulus of the noted phase (m = matrix, p = precipitate), and v_m or v_p as the Poisson's ratio of the noted phase [7].

$$\Delta G_v = \frac{\Delta G_{Al_3X}^{formation} - G_{matrix}^{Al_3X}}{V_{mol}} \quad (2)$$

$$\Delta G_s = \frac{3\varepsilon^2 G_p^{shear} (1 + v_p)}{(1 - 2v_p)} \left[1 - \frac{\left(1 + \frac{3G_m^{shear} (1 + v_m)(1 - v_m)}{(1 - 2v_m)}\right)^{-1} (1 - 2v_p)}{G_p^{shear} (1 + v_p)(1 + v_m)} - \frac{G_m^{shear} (1 + v_m)(1 - 2v_p)}{G_p^{shear} (1 + v_p)(1 - 2v_m)} \right] \quad (3)$$

Because the L_{12} precipitates start to contribute to strengthening effectively at just 1–2 nm [3], it is important to note that the interfacial energy of each precipitate changes based on the precipitate radius. This is because at the smallest radii, only the most favorable (lowest-energy) interfacial planes are used due to the small number of unit cells involved. As the precipitate grows and incorporates more unit cells, it is able to more closely approximate a sphere; this rounding-out results in the use of less-favorable interfacial planes and an increase in average interfacial energy. While differences in interfacial energy for Al_3Sc precipitates have been clearly observed, no clear analysis of the transition has been undertaken. Instead, it has been suggested that a linear increase from the smallest to the largest interfacial energy over the first several nanometers in radius (as in Equation (4)) is sufficient to approximate nucleation and growth trends [8]. In this model, precipitates with radii smaller than 5 nm were made to have size-dependent interfacial energies, while larger precipitates have the maximum interfacial energy (as observed in the literature for overaged precipitates).

$$\gamma = \gamma_{slope\ constant} r_{less\ than\ 5\ nm} + \gamma_{initial} \quad (4)$$

This size dependence complicates matters as calculation of the critical radius of nucleation depends on interfacial energy (Equation (5)). Solving these equations if the critical radius is <5 nm yields Equation (6).

$$r^* = \frac{-2\gamma}{\Delta G_v + \Delta G_s} \quad (5)$$

$$r_{less\ than\ 5\ nm}^* = \frac{-2\gamma_{initial}}{\Delta G_v + \Delta G_s + 2\gamma_{slope\ constant}} \quad (6)$$

The nucleation rate, I , is calculated through the use of Equations (7)–(11), where V_a is the average volume of an atom in the matrix, c is the atomic fraction of solute atoms in the matrix, Z is the Zeldovich factor, β^* is the atomic impingement rate, τ is the incubation time for nucleation, and N_v is the number of nucleation sites per cubic meter (assumed to be the number of solute atoms per cubic meter for homogenous nucleation) [6].

$$V_a = 4ca_p^3 + (1 - 4c)a_m^3 \quad (7)$$

$$Z = \frac{V_a \Delta G_v^2}{8\pi \sqrt{kT} \gamma_{critical\ radius}^3} \quad (8)$$

$$\beta^* = \frac{16\pi c D \gamma_{critical\ radius}^2}{\Delta G_v^2 a_p^4} \quad (9)$$

$$\tau = \frac{8kT a_p^4}{V_a^2 \Delta G_p^2 D c} \quad (10)$$

$$I = N_v Z \beta^* \exp\left[\frac{-4\pi\gamma r^{*2}}{3kT}\right] \exp\left[\frac{-\tau}{t}\right] \quad (11)$$

At this point in the loop, a further nested loop (described in the following section) iterates to grow/dissolve precipitates formed at previous timesteps. After the completion of this loop, the number of solute atoms in precipitates is subtracted from the initial number of solute atoms in the alloy, and the new matrix composition is calculated. The average radius and number of precipitates is also calculated at this point to be used in the calculation of the precipitate strengthening.

For $L1_2$ precipitates such as those found in Al-Sc alloys, the predominant strengthening mechanism at small precipitate size (<3 nm) is order strengthening, which is described in Equation (12). As the average precipitate radius increases over a certain threshold, Orowan strengthening (Equation (13)) gains dominance. By analyzing each of these equations at the end of every time step, it is possible to create a predictive aging curve describing likely strengthening behavior. In these equations, M is the Taylor mean orientation factor, γ_{APB} is the precipitate antiphase boundary energy, b is the Burgers vector of the matrix, f is the phase fraction of precipitates, \bar{R} is the average precipitate radius, and λ_{e-e} is the edge-to-edge interprecipitate spacing [5,16,17].

$$\sigma_{ord} = 0.44 M G_p^{shear} \frac{\gamma_{APB}}{b} f^{\frac{1}{2}} \quad (12)$$

$$\sigma_{or} = \frac{0.4 M G_m^{shear} b^* \ln\left(\frac{2\bar{R}}{b}\right)}{\pi \lambda_{e-e} \sqrt{1 - \nu_m}} \quad (13)$$

It is important to note that Equation (12) has no dependence on λ_{e-e} , while Equation (13) does. In a scenario in which precipitate growth occurs despite a constant phase fraction (such as coarsening), the average strength remains constant until the Orowan strengthening mechanism becomes dominant, at which point the strength begins to decrease. However, in scenarios in which the phase fraction of precipitates increases simultaneously with the average precipitate radius (such as growth during matrix depletion), the increase in strength merely slows down as the average radius increases into the Orowan strengthening regime.

2.1.4. Model Growth/Dissolution Loop

This loop is the innermost nested loop of the model, and it keeps track of any precipitate growth or dissolution that occurs in previously formed precipitates due to solute concentration changes and the Gibbs–Thomson effect. Because it is known how many precipitates, and of which size, were nucleated at each previous timestep, the radius and solute atom content of precipitates formed at each step can be revisited and adjusted. The calculations for each timestep compete for resources (solute atoms), and, as the matrix is depleted of excess solute atoms over the course of the simulation, a near-equilibrium concentration is eventually reached. At this concentration, solute atoms enter precipitates from the matrix at approximately the same rate as they leave them. However, the solute gain/loss ratio of larger precipitates is larger than that of smaller precipitates due to interfacial energy and the Gibbs–Thomson effect. This results in the larger precipitates slowly increasing in size as the smaller precipitates dissolve back into the matrix, a phenomenon commonly referred to as precipitate coarsening.

Precipitate growth in this model is governed by Equation (14), where c_r^m is the equilibrium concentration in the matrix immediately adjacent to a precipitate and c_e^p is the equilibrium concentration of the precipitate. The Gibbs–Thomson effect works on the principle that the equilibrium composition in the matrix immediately adjacent to a precipi-

tate (c_r^m) is affected by the interfacial energy of the precipitate. This effect is described by Equation (15), where c_∞^m is the equilibrium composition at a planar interface [18].

$$\frac{dR}{dt} = \frac{D}{R} \frac{c - c_r^m}{c_e^p - c_r^m} \quad (14)$$

$$c_r^m = c_\infty^m \exp\left(\frac{2\gamma V_m}{R_{gas\ constant} TR}\right) \quad (15)$$

After the innermost loop of the precipitate growth/dissolution at each time step, the solute concentration is updated and applied to the next time loop. After each loop of temperature step, the corresponding temperature-related parameters, such as solubility and diffusivity, are updated. Next, the whole loops move to the next temperature step with the updated information.

2.1.5. Model Outputs

Because of the flexibility afforded by simulating with MATLAB, all inputs, variables, and counters used and/or generated throughout a simulation can be output into Excel. Potentially useful outputs for understanding the precipitation behavior include, but are not limited to: time, temperature, matrix concentration, nucleation rate, precipitate number density, average radius, and the various relevant strengthening mechanisms. The sheer amount of information known about each simulation becomes difficult to display in scientific work, so not all outputs that are discussed in this work are accompanied by a figure.

2.1.6. Model Special Considerations

This model also considers several special considerations due to the circumstances of the physical condition being modeled. For example, in the Al-Sc system, the critical radius is often calculated to be smaller than one unit cell of the precipitate. Since the matrix and precipitate unit cells (FCC Al and L1₂ Al₃Sc) only differ in the substitution of a single Sc atom, there is no possible differentiation between one Al₃Sc unit cell and a unit cell of the matrix with a substitutional Sc atom. Therefore, the critical radius variable was adjusted to never allow predicted precipitates smaller than two unit cells.

Another consideration taken into account is that silicon content can accelerate the kinetics of certain systems, including the Al-Sc system. Si atoms have more favorable bonding with vacancies than Sc atoms. Because Si atoms also tend to cluster with Sc atoms in the Al matrix, the Sc atoms benefit from easier access to vacancies, resulting in an apparent decrease in migration energy (and, in turn, an increased diffusion rate) [13]. This can have a significant effect on precipitation.

Another consideration is the initial incubation state. Classical nucleation theory includes an incubation term, which describes the period required to rearrange homogeneously distributed solute atoms into solute clusters [6]. In this model, it is possible to start the first timestep with the incubation time partially completed, indicating that some clustering has already begun due to room-temperature diffusion or diffusion during initial cooling.

2.2. Experimental Verification Setup

The facilitation of model calibration and accuracy verification required the performance of several experimental trials mirroring heat treatments that were simulated. For these trials, sample charges consisting of master alloys, weighing 600 g in total, were cut and assembled in the proper proportions to achieve the target compositions, as shown in Table 1. All cutting operations were originally performed with a horizontal bandsaw with active cooling, after which the samples were cleaned using an ultrasonic bath of acetone and cut to match specified masses with the use of end-cutting nippers. These charges were then held at 1173 K (900 °C) for 10 min under a 684-Torr atmosphere of ultra-high purity argon and cast into a permanent mold using a vacuum induction melter (VIM). The

permanent mold geometry was designed so that two cylindrical bars were bottom-filled to reduce turbulence within the liquid (Figure 2).

Table 1. Expected and observed alloy compositions.

Alloy (at%)	Target Composition (at%)		ICP-OES Determined (at%)	
	Sc	Si	Sc	Si
Al-0.04Sc	0.04	-	0.041	0.005
Al-0.07Sc	0.07	-	0.068	0.007

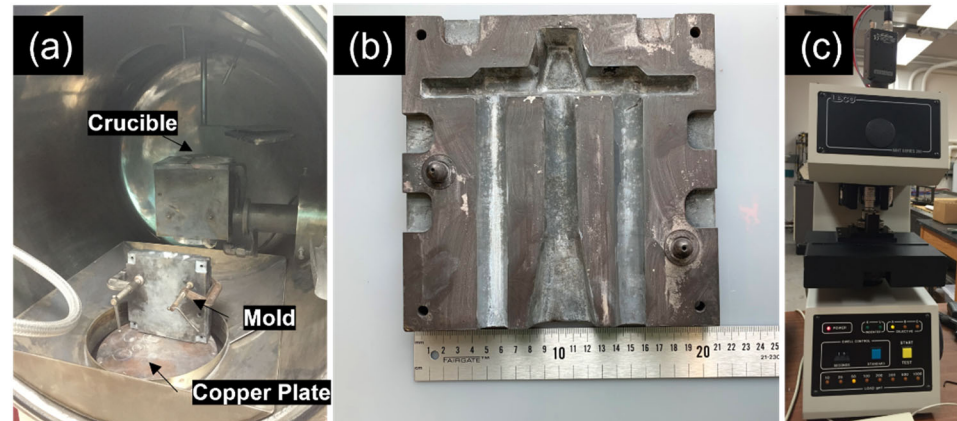


Figure 2. (a,b) The samples for experimental verification were cast into a permanent mold using a vacuum induction melter (VIM). (c) Hardness of the experimental samples was measured using a Leeco Vickers hardness tester.

After casting, holes were drilled into the base of representative bars to create chips for compositional verification using ICP-OES (results shown in Table 1). An optical emission spectrometer (Perkin Elmer Optima 7000DV ICP-OES, PerkinElmer, Inc., Waltham, MA, USA) was used with standards (Inorganic Ventures) to determine the concentrations of the elements of interest (Sc, Si) in each digested solution (College of Forestry, Michigan Technological University, Houghton, MI, USA). For each alloy, a slice approximately 1 cm thick was then removed from the center of a bar using a cutoff wheel and mounted in QuickSet epoxy, Allied High Tech Products, Inc., Compton, CA, USA. The samples were mounted to assist in the initial polishing, but also to create a larger surface to allow adequate gripping during hardness testing. These mounted samples were then ground and polished to a 0.04-micron colloidal silica finish. Once polished, the samples were tested for hardness (Vickers microhardness, 50 g load, 15 s hold, 10 replicates) and conductivity (using a Fischer Technologies Sigmascopie SMP10, Helmut Fischer, Windsor, CT, USA, 10 replicates) to capture baseline conditions.

In order to perform heat treatment at elevated temperatures on the samples, the epoxy had to be removed before each treatment. The samples were broken out of the epoxy mounts by crushing the epoxy in a bench-mounted vice, taking care not to squeeze the epoxy in such a direction as to deform the aluminum sample in the process. Once the sample was broken free, it was heat-treated to match the relevant simulation parameters. After the proper time at temperature, the samples were taken out and immediately quenched to lock in their structure. They were then remounted in epoxy, as discussed in the next paragraph.

Due to the large number of heat treatments required in this study, a method was developed to minimize the need for grinding/polishing on samples that were initially polished. The key to this method was to limit the flow of epoxy under the sample while remounting the sample by covering the bottom of the mounting cup with packaging tape (adhesive facing up) before inserting the sample, polished-side down. Once solidified, the tape and any remaining tape residue were removed from the epoxy-mounted sample, leaving the previously polished surface exposed. With this method, only fine polishing to remove

the oxide layer from the sample would be necessary. In this way, the sample conditions were quickly and efficiently alternated between epoxy-mounted and un-mounted between heat-treatment steps.

The microstructure was investigated in the representative sample using TEM. A thin slice was cut off from the bulk sample using a Japax LUX3 wire electrical discharge machine, Japax, Japan. Several 3-millimeter \varnothing discs were punched from the slices and mechanically ground to $<100 \mu\text{m}$ using SiC paper. The disk samples were polished using a twin-jet polisher with a mixture with a 1:4 ratio of reagent-grade nitric acid to reagent-grade methanol (20 V, $-40 \text{ }^\circ\text{C}$). The precipitate size was characterized using a FEI Titan Themis S-TEM (Thermo Fisher Scientific, Waltham, MA, USA).

2.3. Bayesian Optimization

Assuming a process can be defined by an unknown, continuous objective function f , the goal of BO is to find a global maximizer of this objective function $x^* = \operatorname{argmax}_{x \in X} f(x)$, where X is a design space of interest. In addition, it is assumed that the function f has no simple closed form, but can be evaluated at any arbitrary query point x to obtain the output $y = f(x)$. BO finds the optimum of f by making a series of evaluations, x_1, x_2, \dots, x_T of f , such that the optimum is found in the fewest number of iterations. As more evaluations are observed, BO finds the optimum by sequentially updating the Gaussian process (GP) model [19]. GP is the non-linear probabilistic regression model of the response surface y given the input x . As more data are observed, the shape of the resulting GP surrogate function improves.

2.3.1. Gaussian Process

The primary form of the surrogate function is modeled using a Gaussian process (GP). A GP can be thought of as a distribution over the space of smooth functions where every point in the input space is associated with a Gaussian distributed random variable. Formally, a GP is modeled by

$$f(x) \sim GP(m(x), k(x, x')) \quad (16)$$

where m is the mean function and $k(x, x')$ is the covariance function of any two observations. A popular choice for the covariance function is the squared exponential

$$k(x, x') = \sigma_f^2 \exp\left(-\frac{1}{2l^2}(x - x')^2\right) \quad (17)$$

where σ_f^2 is the output variance and l is the length scale. The output variance σ_f^2 defines the expected deviation of the function output y away from its average value. The length scale l defines the “region of influence” of a point within the parameter space at which the influence of an observation decreases, as one considers points farther away from this observation.

The advantage of using a GP is that it is possible to compute the predictive distribution for a new observation at any location x' . This predictive distribution follows a Gaussian distribution. Its mean and variance are given by:

$$\mu(x') = k(x', X)K(X, X)^{-1}y \quad (18)$$

$$\sigma(x') = k(x', x') - k(x', X)K(X, X)^{-1}k(x', X)' \quad (19)$$

In these equations, a matrix $X = [x_1, x_2, \dots, x_N]$ is denoted and $k(U, V)$ is a covariance matrix whose element (i, j) is calculated as $k_{i,j} = k(x_i, x_j)$ with $x_i \in U$ and $x_j \in V$.

2.3.2. Acquisition Function

Using the GP model above, BO builds a decision function, known as an acquisition function, to select the next point to evaluate, x . An acquisition function determines which parameter settings the next test should use to have the greatest chance of reaching a greater value than previous points. In order to suggest useful points, such an acquisition function considers areas of the GP model in which epistemic uncertainty is high (exploration), as well as areas where the objective function is thought to be high (exploitation).

As the original function $f(x)$ is expensive to evaluate, it is replaced by the acquisition function $\alpha(x)$, which is cheaper. Therefore, instead of maximizing the original function, maximization of the acquisition function is used to select the next point. In this auxiliary maximization problem, the objective $\alpha(x)$ is known and can be easily carried out with standard numerical techniques.

$$x_{t+1} = \operatorname{argmax}_{x \in X} \alpha_t(x) \quad (20)$$

There are many ways to define acquisition functions in the literature. Typically, acquisition functions are designed to seek locations of either high mean and high variance or a combination of the two. In this work, the expected improvement (EI) acquisition function [20,21] which measures the amount of improvement over the best value so far, as used. Formally, the improvement function is defined as $I(x) = \max\{0, f(x) - y^+\}$, where y^+ is the best-observed value so far. Next, the expectation $E[I(x)]$ can be computed analytically as follows. Given $z = \frac{\mu(x) - y^+}{\sigma(x)}$, the EI is computed as:

$$\alpha(x) = [\mu(x) - y^+] \Phi(x) + \sigma(x) \phi(x) \quad (21)$$

where $\mu(x)$ and $\sigma(x)$ are the predictive mean and predictive variance of the Gaussian process described in the previous section, while $\Phi(x)$ and $\phi(x)$ are the normal cumulative distribution function (c.d.f.) and the normal probability distribution function (p.d.f.), respectively.

2.3.3. Illustration of Bayesian Optimization, Gaussian Process, and Acquisition Function

A simple example of how GP is used to describe BO surrogate functions is shown in Figure 3. With experimental knowledge of several points along with the function, sections of the function near to those points have relatively small ranges of probable values, whereas areas that are far from previously sampled points have more variance and, therefore, potentially higher output values. It is also important to note that areas with high variance are not alone in their potential to have local maxima; locations where the variance is small and the means are expected to be high frequently appear as maxima are identified (exploitation).

In this work, BO was first used to minimize the root-mean-square error between precipitate strengthening observed experimentally for specific two-step heat treatments and precipitate strengthening predicted using the KWN model. To achieve a better fit, precipitate-matrix interfacial energy values at nucleation and at $r = 5$ nm were adjusted. Such interfacial values have been determined multiple times in literature, but there is little agreement other than an acknowledgment that the interfacial energy for Al_3Sc decreases at a very small precipitate size due to the preferential formation of interfaces along the lowest energy planes (100). The two-step heat treatments were chosen at the low end of temperatures where Sc is mobile in Al, in an attempt to make the heat-treatment predictions more accurate. Once the KWN model was properly fitted and verified, BO was again used to maximize the strengthening results after heat treatments with limited durations by changing the heat-treatment temperature and simulated heat-treatment step times.

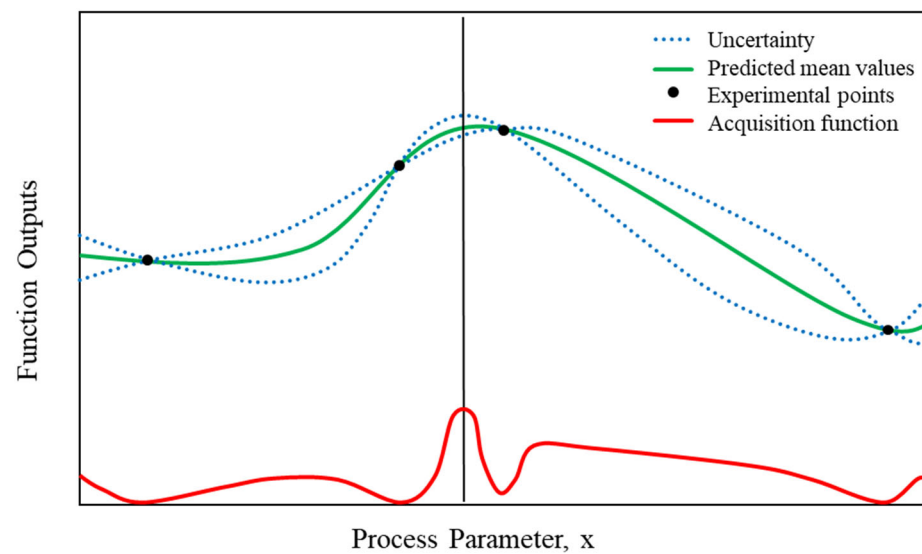


Figure 3. Conceptual representation of a one-dimensional Gaussian process, where several points are defined due to experimental testing of the relevant process. The blue and green lines represent the uncertainty and predicted mean values of the objective function, respectively. The red line represents the acquisition function, and the vertical black line denotes the next requested experimental point.

3. Results and Discussion

The experimental flow of the model optimization and experimental verification is shown in Figure 4. After the Bayesian optimization of the KWN model, the precipitation strengthening was experimentally verified and compared to the predicted results at several selected steps.

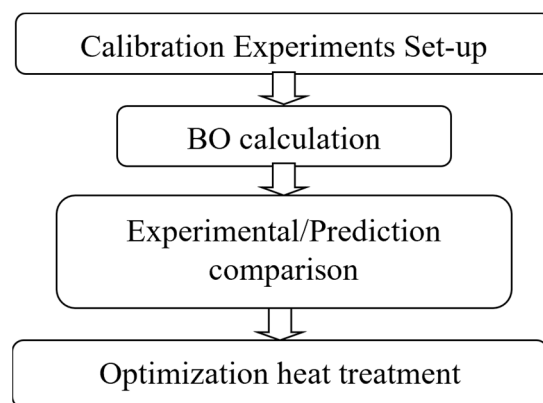


Figure 4. Flow chart of the model optimization and experimental verification.

3.1. Bayesian Optimization of the Precipitation and Strengthening Model

In order to provide initial datasets for the calibration of the model with Bayesian optimization (BO), several two-step heat treatments were performed with Al-0.04Sc at% and Al-0.07Sc at%, varying both the time and temperature held at each step, as described in Table 2.

Upon running a BO routine to determine the best possible fit through the adjustment of the surface energy variables, the ideal values were found and tabulated in Table 3. These values were similar to the values retrieved from the literature.

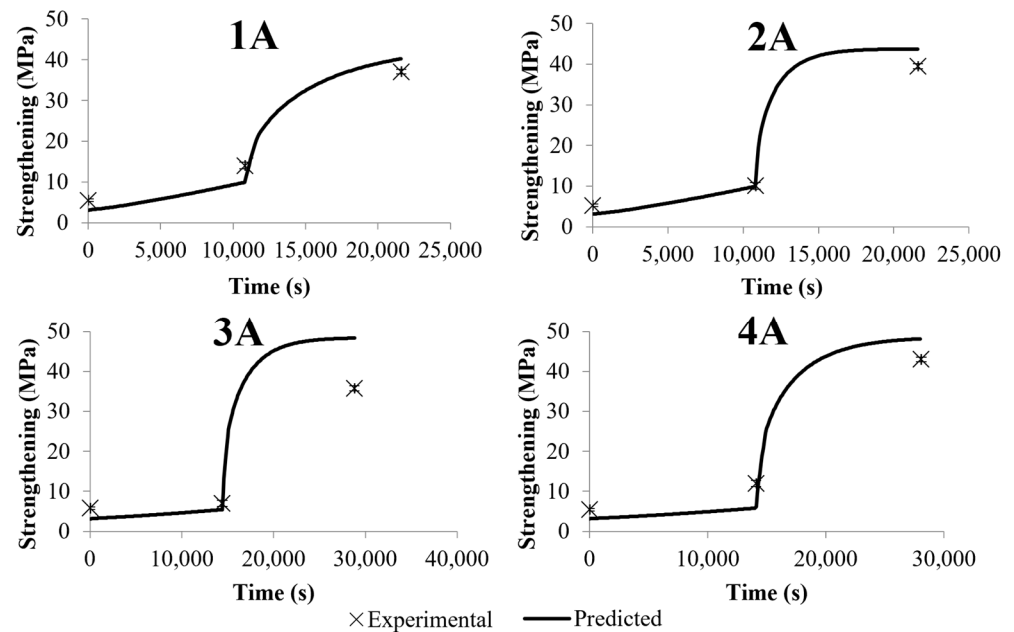
Table 2. Heat-treatment parameters of calibration experiments.

Sample	Alloy (at%)	Heat-Treatment Step 1 (T ₁)		Heat-Treatment Step 2 (T ₂)	
		Temperature (K)	Time (s)	Temperature (K)	Time (s)
1A	Al-0.04Sc	548	10,800	598	10,800
2A	Al-0.04Sc	548	10,800	623	10,800
3A	Al-0.04Sc	518	14,400	608	14,400
4A	Al-0.04Sc	521	14,091	603	13,971
1B	Al-0.07Sc	548	10,800	598	10,800
2B	Al-0.07Sc	548	10,800	623	10,800
3B	Al-0.07Sc	531	14,400	623	7200
4B	Al-0.07Sc	525	14,308	583	9171

Table 3. Comparison of research and BO-Fitted Al: Al₃Sc surface energies and migration energy of Sc in Al.

Reference	Surface Energy (J/m ²)		Migration Energy (eV/atom)	Method
	Nucleation	Coarsening		
Bayesian Optimized	0.096	0.158	0.63	BO
Hyland, 1992 [22]	0.094	-	-	Experimental
Mao, 2011 [23]	-	0.165	-	DFT
Booth-Morrison, 2012 [13]	-	-	0.45–0.74	DFT

A comparison of the observed and the model-predicted results for these heat treatments can be viewed in Figures 5 and 6. The optimized parameters appeared to result in an acceptable fit to the experimental data. This fit to the experimental data was not perfect, as several of the results slightly over-predicted or under-predicted the experimentally observed strengthening effects (which was most noticeable in Sample 3A). However, the lack of a preferential bias in either direction lends credibility to the assumption that experimental error was likely a contributing factor.

**Figure 5.** Graphs demonstrating the experimental and simulated results of several two-step heat treatments for Al-0.04Sc at%, as described in Table 2. Error bars represent ± 2 standard error.

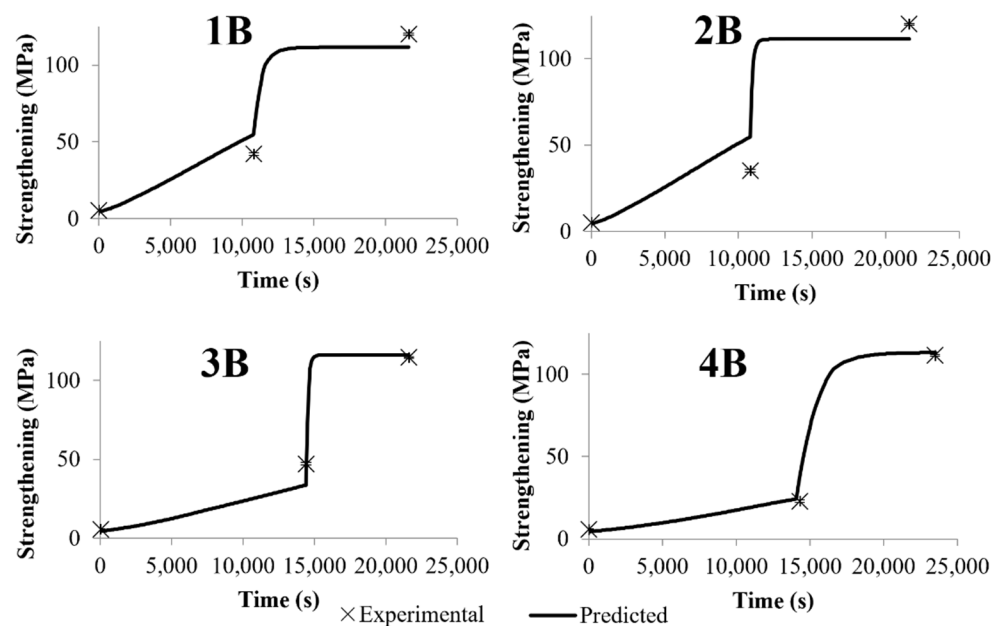


Figure 6. Graphs demonstrate the experimental and simulated results of several two-step heat treatments for Al-0.07Sc at%, as described in Table 2. Error bars represent ± 2 standard error.

3.2. Analysis of Simulation Trends

For each simulation discussed in Section 3.1, an apparent plateau in strengthening was observed in the second step, approximately 50 MPa for Al-0.04Sc at% and 120 MPa for Al-0.07Sc at%. By plotting relevant model variables for each simulation (such as for sample 2A, shown in Figure 7), the cause of the plateau can be determined. In all of these simulations (1A–4B), a similar chain of events preceded the strengthening plateau:

1. During the first heat-treatment step (T_1), the nucleation rate and precipitate growth rate maintained a relatively constant order of magnitude. The matrix concentration declined only slightly due to these effects, which were themselves due to the relatively slow rate of depletion corresponding with the precipitate formation of radii of 1 nm or less.
2. At the onset of the second step (T_2), the nucleation rate immediately dropped by several orders of magnitude, and the rate of precipitate growth increased significantly.
3. As the pre-existing precipitates grew throughout the second step, the matrix became depleted at an accelerated rate and approached the equilibrium solubility at T_2 .
4. As the matrix approached the equilibrium concentration, the nucleation rate and precipitate growth rate decreased until they were nearly negligible, as both were driven by matrix depletion.
5. As the precipitates were no longer changing significantly in size or in number, all the predicted strengthening mechanisms plateaued.

From the preceding events, the lower temperature step (T_1) promoted nucleating Al₃Sc precipitates in the supersaturated solution while limiting the precipitates' growth. The higher temperature step (T_2) was beneficial for growing Al₃Sc precipitates from the nuclei, but the temperature was sufficiently low to limit the coarsening once the supersaturation was depleted. This acceleration in precipitate growth and supersaturation depletion led to larger strength increases upon the completion of the T_2 aging step.

It should also be noted that the average radius reached in sample 2A clearly exceeded the optimal target of 1–3 nm for order strengthening, resulting in the unfortunate dominance of the Orowan strengthening mechanism. This was the case in all the initial simulations (1A–4B). Throughout these tests, the difference in strengthening effect between the predicted Orowan and ordered mechanisms was consistently lower at the conclusion of the Al-0.07Sc at% simulations than in the Al-0.04Sc at% (~10 MPa versus ~50 MPa). This

phenomenon can be linked directly to the fact that the average precipitate radius predicted for the Al-0.04Sc at% was consistently higher than for the Al-0.07Sc at%, which can in turn be linked to the consistently smaller precipitate number density at the end of t_1 within these simulations. Therefore, heat-treatment adjustments aiming to increase precipitate number density should increase the strength. The precipitate sizes in the Al-0.04Sc at% and Al-0.07Sc at% were investigated using TEM. The measured precipitate size in the Al-0.04Sc at% showed higher values than in the Al-0.07Sc at% (8.7 ± 0.5 nm vs. 3.7 ± 0.3 nm) after the two-step heat treatment. This helps to support the trend analysis.

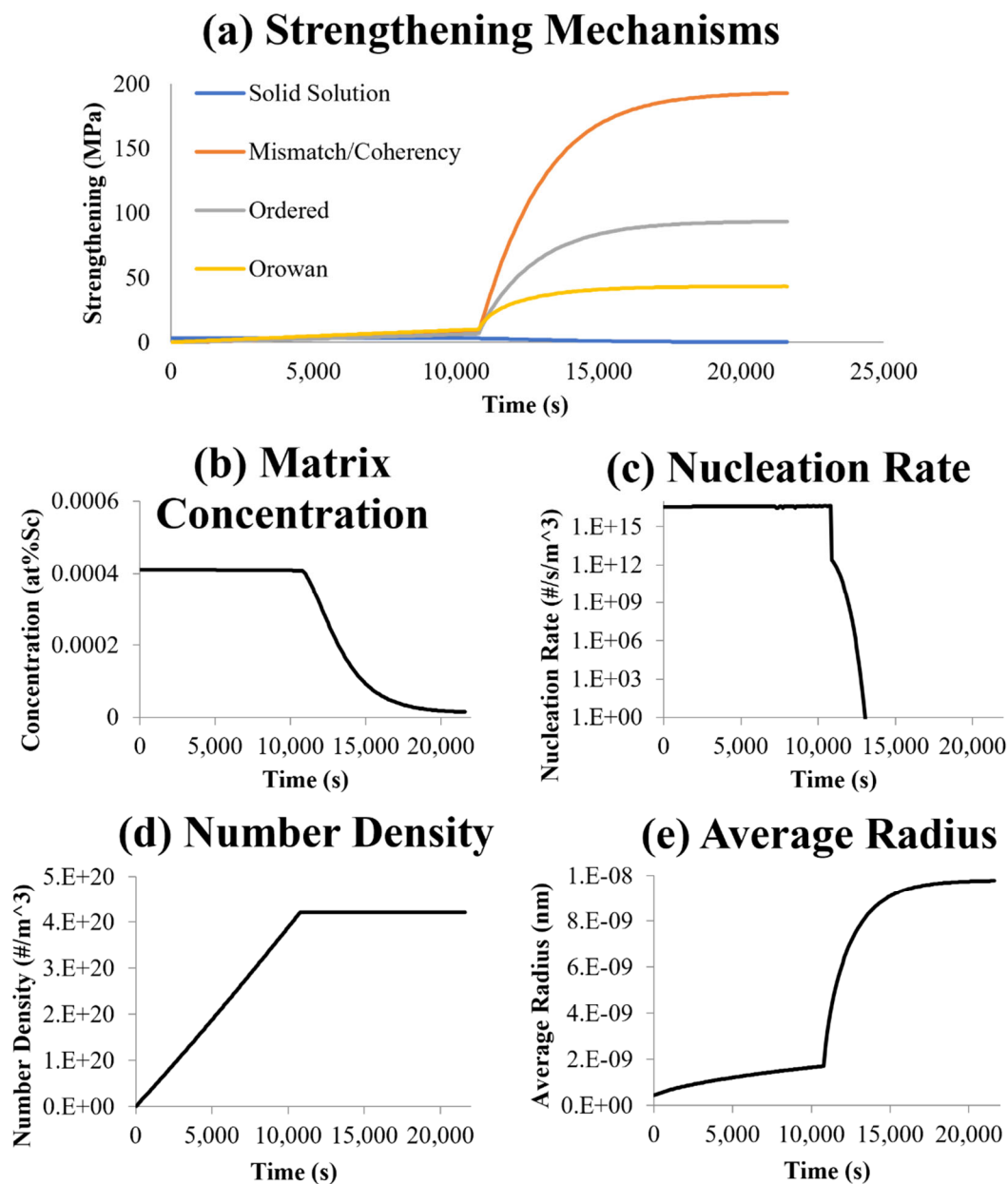


Figure 7. Graphs representing simulation outputs for Sample 2A (described in Table 2 and Figure 5). Throughout the simulated heat treatment, these outputs show (a) the predicted strengthening effect if various strengthening mechanisms are dominant, (b) the concentration of Sc atoms in solution in the matrix, (c) the simultaneous nucleation rate of new precipitates, (d) the number density of existing precipitates in the sample, and (e) the average radius of all existing precipitates.

3.3. Optimized Heat Treatments with No Imposed Time Limit

Figure 8 shows the simulation results for the aging Al-0.04Sc at% for 1×10^6 s at 523 K (250 °C). Long-term heat treatment simulations were also run for the Al-0.07Sc at% at 548 and 573 K (275 and 300 °C). These simulations suggest that holding at T_1 for significantly longer times than in Simulations 1A–4B (from Table 2) resulted in enough depletion in the matrix to effectively halt the nucleation rate. It was also noted that changing the alloy composition and T_1 temperature affected the total possible number of precipitates, which should in turn affect the possible precipitate radius and strengthening.

With the assumptions that the number of precipitates does not change after t_1 given a proper T_2 selection (as supported by the simulations), and that all the remaining matrix supersaturation is depleted during the heat treatment at T_2 through the growth of pre-existing precipitates, Equations (22) and (23) predict what the final average radius would be if, at any given time during heat treatment at T_1 , the sample was switched to T_2 . Figure 9 shows how the predicted average radius after sufficient T_2 varies by changing the time and temperature of the T_1 heat-treatment step for Al-0.04Sc at% and Al-0.07Sc at% with T_1 varying between 523 and 573 K (250 and 300 °C). As an example of how to read these graphs, heat-treating Al-0.04Sc at% at $T_1 = 548$ K for 10,000 s and then switching to $T_2 = 573$ K until full matrix depletion should result in a final average radius of 10 nm.

$$\left(\frac{\#Sc\ atoms}{precipitate}\right)_{after\ T_2} = \left(\frac{\#Sc\ atoms}{precipitate}\right)_{t,T_1} + \frac{\left(\frac{\#Sc\ solute\ atoms}{volume}\right)_{t,T_1} - \left(\frac{\#Sc\ solute\ atoms}{volume}\right)_{eq}}{\left(\frac{\#precipitates}{volume}\right)_{t,T_1}} \quad (22)$$

$$\hat{R}_{after\ T_2} = \left(\hat{R}_{t,T_1} + \frac{3}{4\pi} * \frac{a_{Al_3Sc}^3}{(\#Sc\ atoms)_{unit\ cell}} * \frac{\left(\frac{\#Sc\ solute\ atoms}{volume}\right)_{t,T_1} - \left(\frac{\#Sc\ solute\ atoms}{volume}\right)_{eq}}{\left(\frac{\#precipitates}{volume}\right)_{t,T_1}}\right)^{\frac{1}{3}} \quad (23)$$

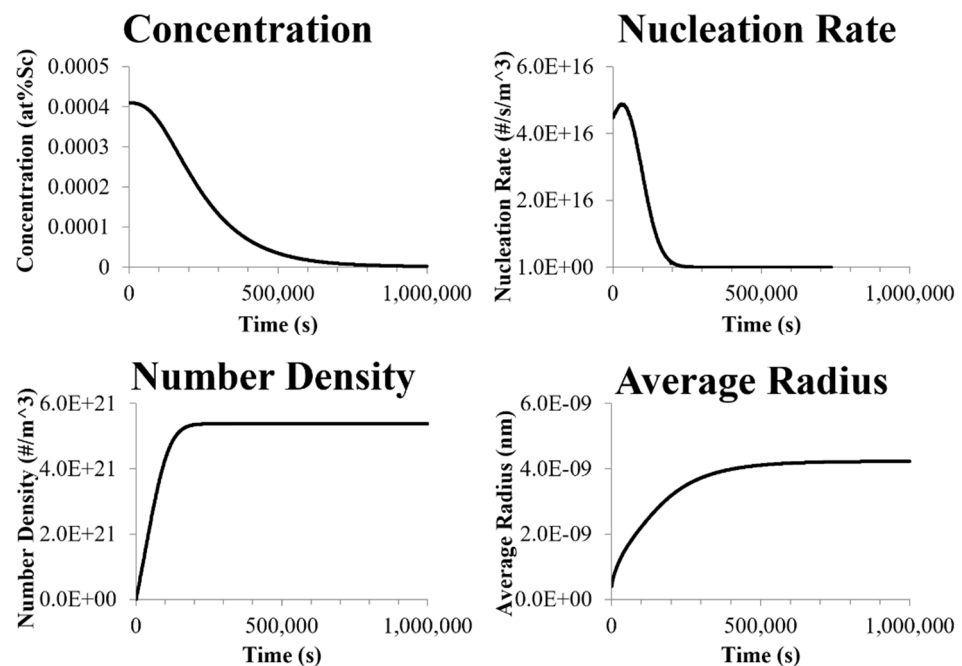


Figure 8. Simulated results for aging Al-0.04Sc at% for 1×10^6 s at 523 K (250 °C), similar to Figure 7. Note that nucleation effectively halts as Sc is depleted from the matrix.

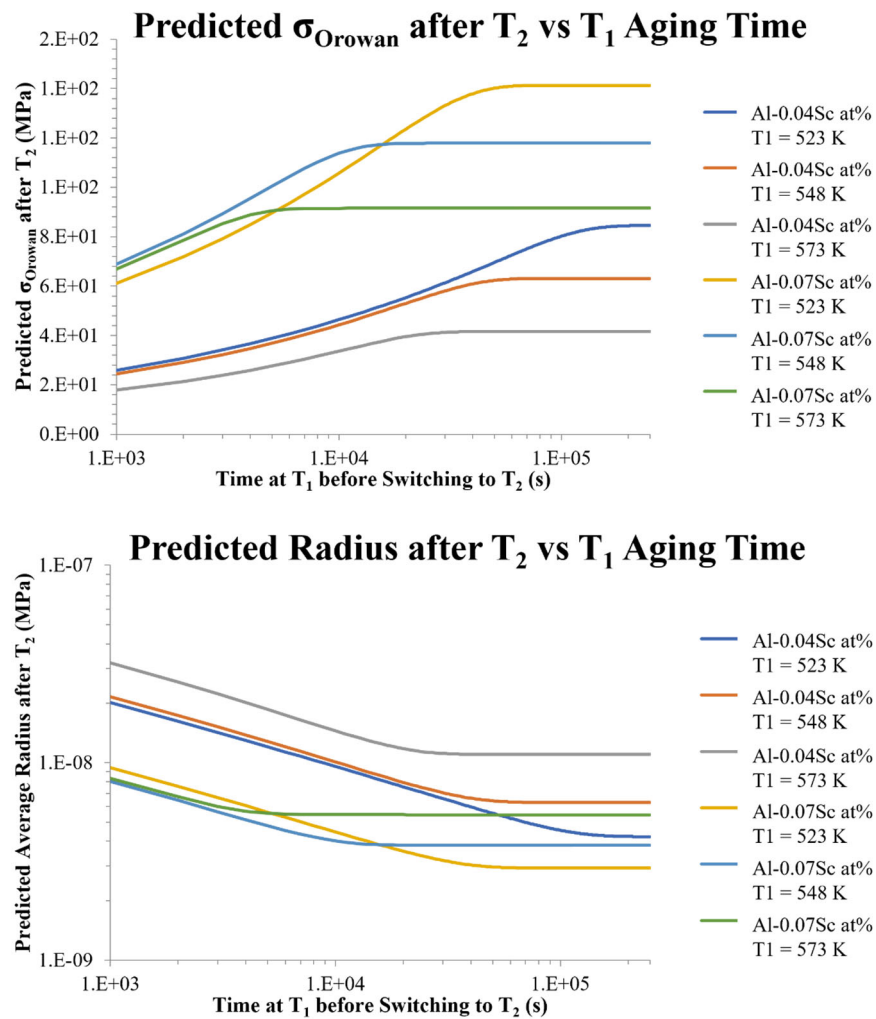


Figure 9. Graphs demonstrating how varying the time and temperature of the first heat treatment step (t_1 and T_1 , respectively) affect the predicted precipitate size and Orowan strengthening after heat treating at a second heat-treatment temperature (T_2) that is sufficiently high to completely deplete excess solute atoms in the matrix.

There are several notable trends in Figures 8 and 9, as discussed below:

1. All long t_1 heat treatments eventually reach an equilibrium, where nucleation effectively stops. At this point, no amount of additional heat treatment can continue to decrease the predicted final radius after T_2 , because the final average radius depends on the Sc atom-to-precipitate ratio. Ideal heat treatments should reach this equilibrium before moving to T_2 .
2. When heat-treated at the same T_1 until matrix depletion, Al-0.04Sc at% always results in larger average precipitates than Al-0.07Sc at%, as fewer precipitates can nucleate in alloys with lower concentration. Heat treatments of alloys with varying Sc content should take this into account.
3. Heat treating at the lowest tested T_1 of 523K (250 °C) requires more time than 548 or 573 K (275 or 300 °C), but it yields the highest strength. This is because, while the nucleation rates are similar between the three temperatures, considerably more precipitate growth occurs in the two higher temperatures. This results in larger precipitates at the end of t_1 and in the more rapid depletion of the matrix. This rapid depletion accelerates the decline in the nucleation rate, limiting the final number of precipitates. Ideal heat treatments should be performed at low initial temperatures, such as 523 K (250 °C), for times that are sufficient to allow maximum strengthening.

- Between these two alloys, only Al-0.07Sc at% at 523 K (250 °C) achieved the target final average radius and, therefore, the maximum potential strengthening associated with the ordered strengthening mechanism. Ideal Al-Sc alloys for heat treatment should be of a concentration \geq Al-0.07Sc at%, and, therefore, be able to achieve the maximum potential strengthening.

To verify these results, several long t_1 simulations and experimental heat treatments were performed, as shown in Figure 10 and described in Table 4. Hardness testing was performed on the experimental samples and resulted in observed precipitate strengthening approximately equal to the predicted strengthening of the model. This supports the hypothesis that increasing the number density of precipitates with a significantly longer t_1 step results in a decrease in the average precipitate radius upon the depletion of the matrix. These results also demonstrate that substantial heat-treatment time savings can be achieved through the use of a second heat treatment step at a slightly higher temperature, in this case 573 K (300 °C), to allow the rapid depletion of the matrix without significant coarsening. However, these heat treatments are still prohibitively long for industrial use.

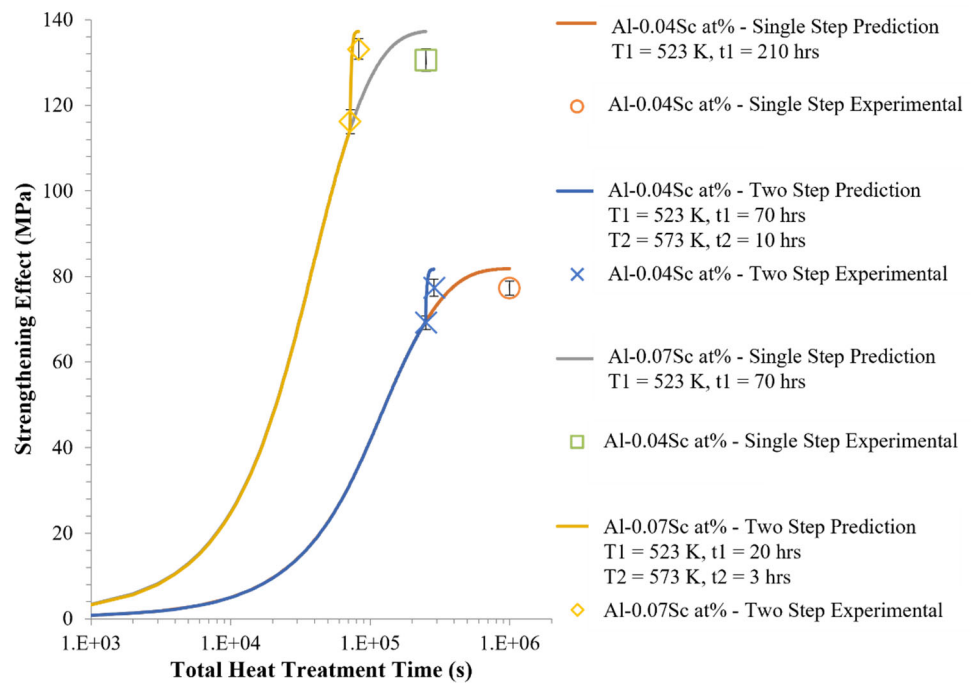


Figure 10. Graphs comparing the observed strengthening effects (via Vickers microhardness tests) and the corresponding model-predicted Orowan strengthening effects in several long heat treatments (Table 4). Error bars represent ± 2 standard error.

Table 4. Long t_1 heat treatments and simulations.

Description	1st Step		2nd Step		Final Strength (MPa)		
	T ₁ (K)	t ₁ (h)	T ₂ (K)	t ₂ (h)	Simulated	Observed	
						Value	2 Std Error
0.04Sc at%, 1 Step	523	210	-	-	82	77	2
0.04Sc at%, 2 Step	523	70	573	10	82	77	2
0.07Sc at%, 1 Step	523	70	-	-	137	131	3
0.07Sc at%, 2 Step	523	20	573	3	137	133	2

The Bayesian optimization not only increased the efficiency of the heat treatment, but also helped with the accuracy of the strengthening prediction. Compared to the general Orowan strengthening predictions for the Al-Sc or similar Al-Sc-Zr alloys containing similar

precipitate sizes (~5 nm), the Bayesian-optimized Orowan strengthening provided the most accurate predictions of the strength increase (Table 5).

Table 5. Accuracy of strengthening predictions using/not using Bayesian optimization.

	Experimental Strength	Predicted Strength	Accuracy	Ref
Al-0.07Sc at%	131	137	96%	Present
Al-0.18Sc at%	140	160	87%	[3]
Al-0.4Sc-0.4Zr at%	500	630	80%	[24]

3.4. Optimized Heat Treatments with Imposed Time Limits

In situations in which heat treatments spanning several days are not feasible, and a target heat-treatment time is imposed, it is useful to predict the optimal heat-treatment temperatures. With this goal in mind, BO processes were again employed, this time to adjust the heat-treatment step times and temperatures and achieve the maximum strengthening effect possible. Table 6 demonstrates the results of one such optimization, and Figure 11 shows a comparison of the corresponding simulations and experimental verification data. From these data, it is apparent that greater t_1 times yield better results, as the optimized time is identical to the upper limit. Furthermore, because the theoretical maximum number of precipitates for ideal temperatures is not reached in these truncated heat treatments, the optimized temperatures for T_1 simply represent the temperatures with the highest nucleation rates.

Table 6. Example Bayesian optimization limits and optimized results.

Alloy (at%)	Upper Time Limit (s)		Optimized Time (s)		Optimized Temp (K)	
	t_1	t_2	t_1	t_2	T_1	T_2
Al-0.04Sc	10,800	14,400	10,800	6936	532	641
Al-0.07Sc	10,800	14,400	10,800	5733	543	592

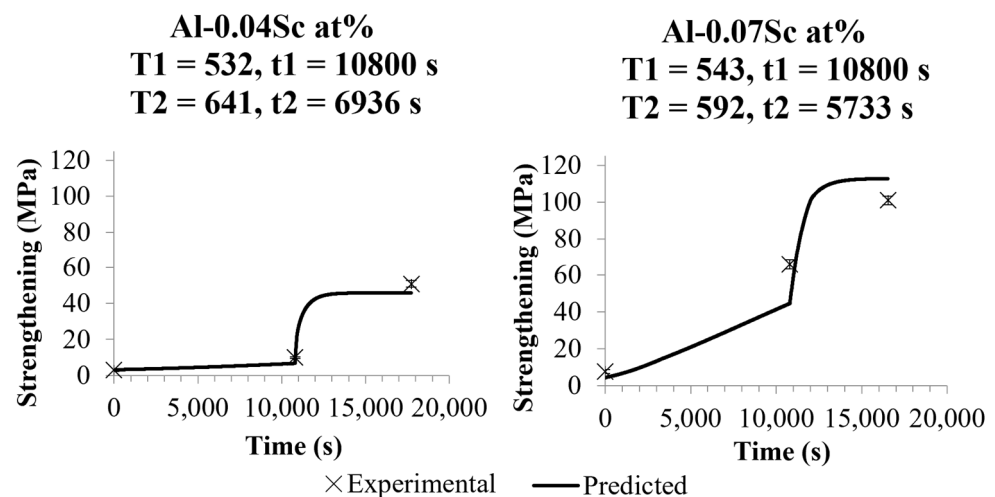


Figure 11. Graphs comparing the predicted and experimental results for heat treatments that were optimized to achieve the greatest strength in a restricted amount of time. In this case, t_1 and t_2 were limited to 3 h each. In both cases, optimal strengthening at T_2 occurred before 3 h. Error bars for experimental points represent ± 2 standard error.

4. Conclusions

In this study, a model was developed to predict the strength of Al-Sc alloys after multiple successive heat treatment steps. The use and theory of this model are described in Section 2.1, and the MATLAB code itself is annotated and included in the Supplementary

Material. Using the Bayesian optimization (BO) of the relevant precipitate-matrix interfacial energy values in order to adjust the model predictions to more closely match the experimental results, the surface energy values for the Al_3Sc at the onset of nucleation and during coarsening were predicted to be 0.096 and 0.158 J/m^2 , respectively. These values were similar to the initial values that were found in the literature (0.094 and 0.165 J/m^2). The model fits the experimental data relatively well, although some errors were observed.

Through the analysis of the model simulations, some guidelines for obtaining the maximum achievable strengthening in these alloys were found:

1. In Al-Sc alloys that do not achieve order strengthening dominance, the greatest strength can be achieved by minimizing the final average radius. This can be achieved by initially holding at a heat treatment temperature with ample nucleation activity and minimal growth activity (e.g. 523 K) until the nucleation rate is negligible due to decreasing supersaturation. At this point, the maximum number of precipitates possible has been reached, and continuing heat treatment at this temperature, or at a reasonably high temperature (e.g. 573 K) results in a minimal average radius.
2. Ideally, two heat-treatment steps should be used for Al-Sc alloys, as full the depletion of the matrix after the initial nucleation treatment at proper nucleation temperatures can be prohibitively time-consuming. Adding a short second step at a higher temperature can significantly decrease the total required time.
3. Sc concentrations greater than Al-0.07Sc at% are suggested in order for the Sc additions to achieve their full potential. The simulations showed that increasing the solute concentration decreased the final achievable average sizes of the precipitates by allowing a greater comparative number density of the precipitates to be nucleated. An alloy with Al-0.04Sc at% is predicted to be unable to produce precipitates small enough to allow ordered strengthening dominance, while the Al-0.07Sc at% was predicted to be able to form small enough precipitates in only a minority of circumstances (e.g., $T_1 = 523 \text{ K}$, $t_1 = 10 \text{ h}$).

Considering that long, low-temperature heat treatments are not always possible in an industrial setting, the BO of the model can also be used to determine the ideal strengthening time and temperature parameters given the upper time limits. For the demonstrated examples, the maximum achievable strength was considerably lower than the strength that would have been possible with the long, low-temperature heat treatments, but the computer-optimized temperature parameters succeeded in predicting a slightly stronger final strength than could be achieved with more traditional, rounded temperature values. This demonstrated that the approach could be repurposed for other time limitations, etc., if required. However, designing heat treatments by determining the time required to nucleate the maximum number of precipitates through simulation generally results in greater strengthening.

Supplementary Materials: The following are available at: <https://www.mdpi.com/article/10.3390/met12060975/s1>. The MATLAB code for the calculations used in this work is included in a separate file in the Supplementary Materials.

Author Contributions: Funding acquisition, P.G.S.; investigation, K.D., Y.Y. and V.N.; methodology, K.D. and P.G.S.; supervision, P.G.S.; writing—original draft, K.D.; writing—review and editing, Y.Y., J.J.L., S.R., S.G., S.V. and P.G.S. All authors have read and agreed to the published version of the manuscript.

Funding: This work was funded by the Office of Naval Research, grant no. N00014-11-10876.

Institutional Review Board Statement: Not applicable.

Informed Consent Statement: Not applicable.

Data Availability Statement: Not applicable.

Acknowledgments: The authors acknowledge the Applied Chemical and Morphological Analysis Laboratory at Michigan Tech for use of the instruments and staff assistance.

Conflicts of Interest: The authors declare no conflict of interest. The funders had no role in the design of the study; in the collection, analyses, or interpretation of data; in the writing of the manuscript, or in the decision to publish the results.

References

1. Knipling, K.E.; Dunand, D.C.; Seidman, D.N. Criteria for developing castable, creep-resistant aluminum-based alloys: A review. *Z. Für Met.* **2006**, *97*, 246–265. [[CrossRef](#)]
2. Knipling, K.E.; Seidman, D.N.; Dunand, D.C. Ambient-and high-temperature mechanical properties of isochronally aged Al–0.06 Sc, Al–0.06 Zr and Al–0.06 Sc–0.06 Zr (at.%) alloys. *Acta Mater.* **2011**, *59*, 943–954. [[CrossRef](#)]
3. Seidman, D.N.; Marquis, E.A.; Dunand, D.C. Precipitation strengthening at ambient and elevated temperatures of heat-treatable Al (Sc) alloys. *Acta Mater.* **2002**, *50*, 4021–4035. [[CrossRef](#)]
4. Marquis, E.A.; Seidman, D.N. Nanoscale structural evolution of Al₃Sc precipitates in Al (Sc) alloys. *Acta Mater.* **2001**, *49*, 1909–1919. [[CrossRef](#)]
5. Knipling, K.E.; Karnesky, R.A.; Lee, C.P.; Dunand, D.C.; Seidman, D.N. Precipitation evolution in Al–0.1 Sc, Al–0.1 Zr and Al–0.1 Sc–0.1 Zr (at.%) alloys during isochronal aging. *Acta Mater.* **2010**, *58*, 5184–5195. [[CrossRef](#)]
6. Wagner, R.; Kampmann, R.; Voorhees, P. Homogeneous Second-Phase Precipitation. In *Phase Transformations in Materials*; Kostorz, G., Ed.; Wiley-VCH Verlag GmbH & Co. KGaA: Weinheim, Germany, 2001; pp. 309–480.
7. Robson, J.D. Modelling the overlap of nucleation, growth and coarsening during precipitation. *Acta Mater.* **2004**, *52*, 4669–4676. [[CrossRef](#)]
8. Robson, J.D.; Jones, M.J.; Prangnell, P.B. Extension of the N-model to predict competing homogeneous and heterogeneous precipitation in Al–Sc alloys. *Acta Mater.* **2003**, *51*, 1453–1468. [[CrossRef](#)]
9. Shahriari, B.; Swersky, K.; Wang, Z.; Adams, R.P.; de Freitas, N. Taking the human out of the loop: A review of bayesian optimization. *Proc. IEEE* **2015**, *104*, 148–175. [[CrossRef](#)]
10. Dai Nguyen, T.; Gupta, S.; Rana, S.; Nguyen, V.; Venkatesh, S.; Deane, K.J.; Sanders, P.G. Cascade Bayesian Optimization. In *Australasian Joint Conference on Artificial Intelligence*; Springer International Publishing: Berlin/Heidelberg, Germany, 2016; pp. 268–280.
11. Nguyen, V.; Rana, S.; Gupta, S.K.; Li, C.; Venkatesh, S. Budgeted batch Bayesian optimization. In Proceedings of the Data Mining (ICDM), 2016 IEEE 16th International Conference on IEEE, Barcelona, Spain, 12–15 December 2016; pp. 1107–1112.
12. Murray, J.L. Al–Sc (aluminum-scandium) system. *J. Phase Equilibria Diffus.* **1998**, *19*, 380. [[CrossRef](#)]
13. Booth-Morrison, C.; Mao, Z.; Diaz, M.; Dunand, D.C.; Wolverson, C.; Seidman, D.N. Role of silicon in accelerating the nucleation of Al₃(Sc, Zr) precipitates in dilute Al–Sc–Zr alloys. *Acta Mater.* **2012**, *60*, 4740–4752. [[CrossRef](#)]
14. Manjeera, M. A First-Principles Methodology for Diffusion Coefficients in Metals and Dilute Alloys. Ph.D. Thesis, The Pennsylvania State University, State College, PA, USA, 2008.
15. Introduction of Thermodynamics of Materials–David R. Gaskell. Available online: <https://www.scribd.com/doc/91993285/Introduction-of-Thermodynamics-of-Materials-David-R-Gaskell> (accessed on 4 March 2016).
16. Ardell, A.J. Precipitation hardening. *Metall. Trans.* **1985**, *16*, 2131–2165. [[CrossRef](#)]
17. Courtney, T. *Mechanical Behavior of Materials*, 2nd ed.; Waveland Pr Inc.: Long Grove, IL, USA, 2005.
18. Perez, M. Gibbs–Thomson effects in phase transformations. *Scr. Mater.* **2005**, *52*, 709–712. [[CrossRef](#)]
19. Rasmussen, C.E.; Williams, C.K. *Gaussian Processes for Machine Learning*; MIT Press: Cambridge, MA, USA, 2006.
20. Moćkus, J. On Bayesian methods for seeking the extremum. In *Optimization Techniques IFIP Technical Conference*; Springer: Berlin/Heidelberg, Germany, 1975; pp. 400–404.
21. Nguyen, V.; Gupta, S.; Rana, S.; Li, C.; Venkatesh, S. Regret for Expected Improvement over the Best-Observed Value and Stopping Condition. In Proceedings of the 9th Asian Conference on Machine Learning, Seoul, Korea, 15–17 November 2017.
22. Hyland, R.W. Homogeneous nucleation kinetics of Al₃Sc in a dilute Al–Sc alloy. *Metall. Trans.* **1992**, *23*, 1947–1955. [[CrossRef](#)]
23. Mao, Z.; Chen, W.; Seidman, D.N.; Wolverson, C. First-principles study of the nucleation and stability of ordered precipitates in ternary Al–Sc–Li alloys. *Acta Mater.* **2011**, *59*, 3012–3023. [[CrossRef](#)]
24. Yang, Y.; Licavoli, J.J.; Sanders, P.G. Improved strengthening in supersaturated Al–Sc–Zr alloy via melt-spinning and extrusion. *J. Alloys. Compd.* **2020**, *826*, 154185. [[CrossRef](#)]